TiO2 nanotree films for the production of green H2 by solar water splitting: From microstructural and optical characteristics to the photocatalytic properties

Adeline Miquelot, Olivier Debieu, Vincent R. Rouessac, Christina Villeneuve-Faure, Nathalie Prud'Homme, Jérémy Cure, Vassilios Constantoudis, George Papavieros, Stéphanie Roualdes, Constantin Vahlas

TiO_2 nanotree films for the production of green H_2 by solar water splitting: From microstructural and optical characteristics to the photocatalytic properties

Adeline Miquelot[a], Olivier Debieu[a], Vincent Rouessac[b], Christina Villeneuve[c], Nathalie Prud'homme[d], Jérémy Cure[e], Vassilios Constantoudis[f,g], George Papavieros[f,g], Stéphanie Roualdes[b], Constantin Vahlas[a,*]

[a] *Cirimat, 4 allée Emile Monso, BP-44362, 31030 Toulouse Cedex 4, France*
[b] *IEM, Université de Montpellier, CC 047 - Place Eugène Bataillon, 34095 Montpellier Cedex 5, France*
[c] *Laplace, Université Toulouse 3 - Paul Sabatier, 118, route de Narbonne - bât 3R3 -, 31062 Toulouse cedex 9, France*
[d] *ICMMO, Université Paris Sud, 11-SP2M-Bât, 410-91405 Orsay Cedex, France*
[e] *LAAS, CNRS, Avenue du Colonel Roche, 31031 Toulouse, France*
[f] *NCSR Demokritos, Neapoleos 27 and Patr. Grigoriou str., 15310 Aghia Paraskevi, Attiki, Greece*
[g] *Nanometrisis, TEPA Lefkippos, Patriarchou Grigoriou & Neapoleos 27, PO Box 60037, Agia Paraskevi 15341, Attiki, Greece*

ARTICLE INFO

Keywords:
Solar water splitting
TiO_2
Nanostructure
Photocatalysis
Conductive-AFM
MOCVD

ABSTRACT

Green H_2 production by solar water splitting relies entirely on the intrinsic properties of the photocatalyst. In this study the impact of these intrinsic properties on the photocatalytic activity of anatase TiO_2, the quintessential component of state of the art photocatalytic systems was explored at the nanoscale. The exploration involved a holistic microstructural and optical characterization of fully crystallized anatase thin films synthetized by metalorganic chemical vapor deposition. A combination of electron microscopy, spectroscopic ellipsometry, and infrared spectroscopy revealed that when the deposition temperature increased, the morphology evolved from dense to porous and columnar nanostructures. Interestingly, the columns with a complex, tree-like nanostructure photogenerated 18 times more H_2 than the densest sample. This result shows that the beneficial effect of the morphological nano-complexification and crystallographic diversification of the exchange facets on the photocatalytic performance outweighs the detrimental aspects inherent to this evolution, namely the drop of the charge carrier transport and the increase of residual stress.

1. Introduction

Research on renewable energy is vital in the current context of global warming and societies that rely on high energy consumption. Hydrogen is a promising source of renewable energy and catalyzed solar water splitting (SWS) is a carbon-free method to produce it. Numerous materials have been tested to catalyze this reaction [1,2]. Among them, TiO_2 – because it is non-toxic, chemically stable, abundant and affordable has been widely investigated as a photocatalytic material since Fujishima and Honda's seminal work [3–8]. Despite its high energy band-gap (3.2 eV), crystalline anatase TiO_2 shows attractive opto-electronic properties. It is an indirect semiconductor with a long exciton lifetime [9,10]; it has a conduction band minimum energy level below the redox potential of $H+/H_2$ (0 V *vs.* NHE) and a valence band maximum energy level above the redox potential of O_2/H_2O (+1.23 V *vs.* NHE) [11,12]. In contrast with powders,

Abbreviations: SWS, solar water splitting; ALD, atomic layer deposition; MOCVD, metalorganic chemical vapor deposition; TTIP, titanium tetraisopropoxide; FESEM, field emission scanning electron microscopy; EBSD, electron backscatter diffraction; GIXRD, grazing incidence X-ray diffraction; PF-QNM, peak force quantitative nanomechanical; C-AFM, conductive atomic force microscopy; SE, spectroscopic ellipsometry; SEP, spectroscopic ellipsometric porosimetry; HRTEM, high resolution transmission electron microscopy; MUD, multiples of uniform distribution; LO, longitudinal optical; TO, transverse optical; CL, correlation length

* Corresponding author.
E-mail addresses: adeline.miquelot@ensiacet.fr (A. Miquelot), olivier.debieu@ensiacet.fr (O. Debieu), vincent.rouessac@umontpellier.fr (V. Rouessac), christina.villeneuve@laplace.univ-tlse.fr (C. Villeneuve), nathalie.prudhomme@u-psud.fr (N. Prud'homme), jcure@laas.fr (J. Cure), v.constantoudis@nanometrisis.com (V. Constantoudis), g.papavieros@nanometrisis.com (G. Papavieros), stephanie.roualdes@umontpellier.fr (S. Roualdes), constantin.vahlas@ensiacet.fr (C. Vahlas).

https://doi.org/10.1016/j.apsusc.2019.07.191

anatase TiO_2 films can be used in photocatalysis as well as in electro-photocatalysis. They are produced by various methods: sol-gel [13], anodization [14], reactive magnetron sputtering [15], atomic layer deposition (ALD) [16] or metalorganic chemical vapor deposition (MOCVD) [4,17,18]. This last process interestingly enables the production of various hierarchical morphologies that have an impact on the photocatalytic properties [5,19].

One way to efficiently control the morphology is the deposition temperature (T_d), which allows obtaining nano- or microstructures that range from dense to columnar [20–22]. Such T_d induced nanostructuration results in the increase of the specific surface area and therefore enhances the photocatalytic activity [23]. However, an increase in T_d can concomitantly affect other properties, such as the texture, the electrical transport, the residual stress, and the nature of the external crystallographic facets in contact with the aqueous solution. These factors can either enhance or be detrimental to the photocatalytic activity [23–27]. Other aspects such as the stoichiometry can also influence the photocatalytic performance through the subsequent modification of the electronic properties.

A significant number of results has been reported on the determination of the morphology [16,18,28,29], the crystallographic phases [22], the mechanical residual stress [26,30], the purity [2], the electrical transport [9], and the optical band-gap [31]. However, there is no systematic, holistic study of TiO_2 films in the context of a strong morphology evolution that connects all of these characteristics to the evolution of their photocatalytic properties. The present work thus, focuses on an extended characterization of MOCVD anatase TiO_2 films in order to investigate their photocatalytic behavior and thereby improve the photocatalytic performance by monitoring deposition parameters. The outcomes of this work can be extended to nanostructured TiO_2 films synthesized by other techniques.

We deposit TiO_2 films by thermally activated MOCVD from titanium tetraisopropoxide (TTIP) at six temperatures between 325 and 500 °C. We quantify the surface morphology of the deposited films through image processing and analysis of field emission scanning electron microscopy (FESEM) micrographs. We apply, for the first time, electron backscatter diffraction (EBSD) to determine the growth direction of the anatase films. We determine the intrinsic mechanical residual stress of the films and their evolution with T_d by grazing incidence XRD (GIXRD), and we probe the mechanical properties at the nanoscale by peak force quantitative nanomechanical (PF-QNM). The electrical properties are investigated at the nanoscale by conductive atomic force microscopy (C-AFM) and at the macroscale by Hall effect measurements. We fit spectroscopic ellipsometry (SE) measurements using the Cody-Lorentz model [32], a powerful tool to determine the thickness, the band-gap, and the refractive index that is affected by the porosity. We correlate the outcome of this comprehensive microstructural, electrical, electronic, and optical study with the photocatalytic activity measured by two techniques. First, we measure the photodegradation of stearic acid catalyzed by the TiO_2 films by Fourier transform infrared (FTIR) spectroscopy, which is a variant of the Pilkington test [33–35]. Second, we measure the H_2 photogeneration under Xe lamp irradiation in a controlled atmosphere by gas chromatography [36].

2. Material and methods

TiO_2 films are deposited in a vertical, cylindrical, stagnant flow cold wall stainless steel MOCVD reactor, which has been described in detail elsewhere [37]. In each experiment, P light-doped (1–20 Ω.cm) and As high-doped (0.001–0.005 Ω.cm) n-type Si (100) wafers, and fused silica windows (Neyco) are placed on the heated sample holder. Titanium tetraisopropoxide (TTIP, 99.999%, Sigma-Aldrich) is conditioned in a double-walled glass bubbler and is thermally regulated at 20.5 °C. Pure nitrogen (99.9999% Messer) is used as both the carrier and dilution gas, and their flow rate is fixed to 4.7 and 52.4 sccm, respectively. All gas lines are thermally regulated at *ca.* 65 °C. Depositions are performed at 1 Torr fixed pressure, at different T_d ranging from 325 to 500 °C, with various durations that are adapted to produce films of similar thicknesses (~350 nm).

Film composition is investigated by X-ray photoelectron spectroscopy (XPS). The photoelectron emission spectra are recorded using a monochromatized Al K_α ($h\nu$ = 1486.6 eV) source on a ThermoScientific K-Alpha system with a 400 µm X-ray spot size. Depth profiling is performed by means of Ar^+ ion etching under 2 keV.

The crystal structure is investigated by XRD in a Bruker-D8 diffractometer equipped with a Cu Kα ($\lambda_{K\alpha Cu}$ = 0.154 nm) anode in theta-theta mode with a −3° offset. In addition, GIXRD is used to determine residual stress using a 4-circles goniometer (Panalytical X'Pert) equipped with a Cu anode ($\lambda_{K\alpha Cu}$ = 0.154 nm) at 40 kV and 40 mA, with Soller slits to get a nearly parallel beam, and a fast recording detector (X'celerator, Panalytical). The $\sin^2\psi$ method (11 ψ angles ranging from −60° to 60°), in one direction (ϕ = 0°), was applied to the samples deposited on fused silica substrates. The {020} family plane (2θ = 48.08°) is analyzed from 45.7° to 51.2° with a 0.066° step, with the step time varying between 2000 and 2700 s depending on the sample. The XRD penetration depth is estimated at 100 nm for dense TiO_2. The *modus operandi* to determine the strain from XRD measurements is explained in the Supplementary Information (SI section 1).

EBSD measurements are performed in a FESEM Jeol JSM 7100F TTLS LV on the sample surface to explore crystalline orientation. 8633, 4604, and 7888 points are measured on the 500 °C, 400 °C, and 325 °C samples, respectively, on 38 μm^2 surfaces. Because each grain is probed only once to avoid overrepresentation of one grain orientation, the distribution remains statistical. Mid-IR (MIR) FTIR and far-IR (FIR) FTIR spectra are recorded by Perkin Elmer Frontier, and Nicolet iS50 ThermoFischer Scientific spectrometers, respectively. Films deposited on fused silica are investigated by transmission, total and diffuse reflectance spectroscopy in the 200–1650 nm spectral range, using an Agilent-Cary 5000 spectrophotometer equipped with an integrating sphere. Samples deposited on Si coupons are analyzed by spectroscopic ellipsometry (SE) in the same spectral range with an incidence angle of 75° using a Semilab SE-2000 apparatus. Spectroscopic ellipsometric porosimetry (SEP) is performed with a Semilab GES5E spectroscopic ellipsometer (250–1000 nm) coupled with a lab-made cell in which ethanol pressure is increased step by step to progressively acquire ellipsometric data adsorption isotherms in almost steady state. Before any data acquisition, the cell is pumped down to 50 mTorr, whereas the sample is heated up to 200 °C in the vacuumed cell for several minutes for a complete desorption from the TiO_2 film. The ellipsometry data are analyzed on the energy range 1.24–4.25 eV by the Semilab SEA software using a two-layer architecture. A Cody-Lorentz oscillator model is used to describe the optical properties of the film, and a Bruggeman effective medium approach is chosen to simulate the surface roughness. With this full optical model, the regression goodness of fit in this range is over 0.98. The Cody-Lorentz model enables us to probe band-to-band transitions at the optical band edge and above the band edge, as well as band tails in the transparent spectral domain.

Top view and cross sectional scanning electron microscopy (SEM) micrographs of the Pt-metalized samples are obtained with a field emission FESEM Jeol JSM 6700F instrument. Before analyzing top view SEM images with the nanoTOPO_SEM™ software provided by Nanometrisis, they are processed to normalize the contrast of their illumination. Transmission electron microscopy (TEM) and high resolution TEM (HRTEM) data are obtained with a JEOL JEM 2100F microscope. TEM specimens are prepared using a FEI Helios Nanolab600i dual beam SEM FIB (focused ion beam). The ion column is operated at 30 kV for all steps except final cleaning of the specimen, where a voltage of 5 kV and 2 kV is used. Beam currents vary between 47 nA and 15 pA. The electron beam is used to deposit a layer of C 200 nm thick over an area of 20 µm × 2 µm. The ion beam was then used to deposit a layer of Pt 3 µm thick over the same area. The sample was lifted out *in situ* and then attached to a copper support grid. Thinning of the specimen

could proceed using a gradual cross-section cleaning milling pattern, with a final milling beam current of 80 pA. Finally, a 5 kV and 2 kV cleaning steps were carried out on each side.

Surface topography is probed by a Bruker Multimode 8 AFM apparatus in PF-QNM mode with Si-tip (Tespa-V2, Bruker). The mechanical deformation is mapped using maximum contact force of *ca.* 65 nN. The tip sensitivity and its spring constant k are determined by force distance curve on Si reference wafer and by thermal tune, respectively. The vertical nanoscale charge transport is locally probed on thin films deposited on highly doped Si wafers by the AFM in conductive mode using a SCM-PtSi (Bruker) tip. A contact force of 27 nN and a sensor sensitivity of 100 nA/V are used. Hall measurements are conducted in a DC magnetic field with AC current from a Keithley 6221 current source and with an amplifier MFLI from Zurich Instruments. The contacts are Cu/Be and the injected current is of the order of 10^{-7} A.

The normalized Pilkington tests follow the photodegradation of stearic acid under UV–visible light (above 355 nm), as described elsewhere [28]. The relative quantity of stearic acid on the TiO_2 films is analyzed every 20 min by following the most intense stearic acid FTIR peak intensity evolution. For each sample, the test is repeated once after water cleaning. After the first run, the 500 °C film is delaminated, in contrast with the others which present perfect integrity. Finally, TiO_2 induced water photodissociation tests are performed in a quartz reactor filled with a water-ethanol solution (1:1 vol) under Xe-lamp (300 W) illumination. The produced H_2 quantity is measured every 6 h with a gas chromatography apparatus connected to the photodissociation reactor (PlotQ column (30 m) and PE-molisieve column (30 m); thermal conductivity detector; carrier gas: Ar).

A substantial effort has been made to ensure that only the final analysis for each sample is destructive or potentially destructive. To this end, both H_2 photogeneration and stearic acid photodégradation are realized on different samples for each T_d, which have not been exposed to other destructive analyses.

3. Results

3.1. Crystallographic phase and texture

The composition of the TiO_2 films, which was determined on a preliminary basis by XPS, showed no other contamination than the classical surface carbon due to adsorption of organic molecules, as revealed by the depth profiles.

Fig. 1a shows XRD patterns obtained in a theta-theta mode, of *ca.* 350 nm TiO_2 films deposited on SiO_2 substrates at the different T_d. In this figure, and in the rest of the text, the following color coding is used: dark blue, light blue, green, yellow, orange, and red for T_d of 325, 350, 375, 400, 450, and 500 °C, respectively.

Peaks measured at 25.4, 38.5, 48.1, 55.1, 62.7, 70.3, 75, and 76° correspond to the (101), (112), (020), (121), (024), (220), (125), and (031) crystallographic planes of anatase, respectively, according to the 99-100-9704 JCPDS powder card depicted for comparison. No peak from rutile or brookite is detected. All diffractograms present different intensity ratios than the powder reference pattern (shown in black), revealing textured films. Diffractograms of films deposited between 325 °C and 400 °C are rather similar, with two major peaks (101) and (020) that increase slightly with increasing T_d. By contrast, diffractograms, of films deposited at 450 °C and 500 °C show a general and significant intensity decrease, along with a change in peak ratio. The (101) and (020) peaks vanish while the (112) and the (220) (Fig. 1b) peaks increase.

Khalifa also reports a general decrease of XRD peak intensity with increasing T_d, especially above 400 °C, for TiO_2 films deposited by MOCVD in similar conditions [22]. In this temperature range, a change also occurs in the relative intensities between the (101) and (112) peaks, with the latter becoming predominant. The author attributes this behavior to the decrease of the migration length of the precursor

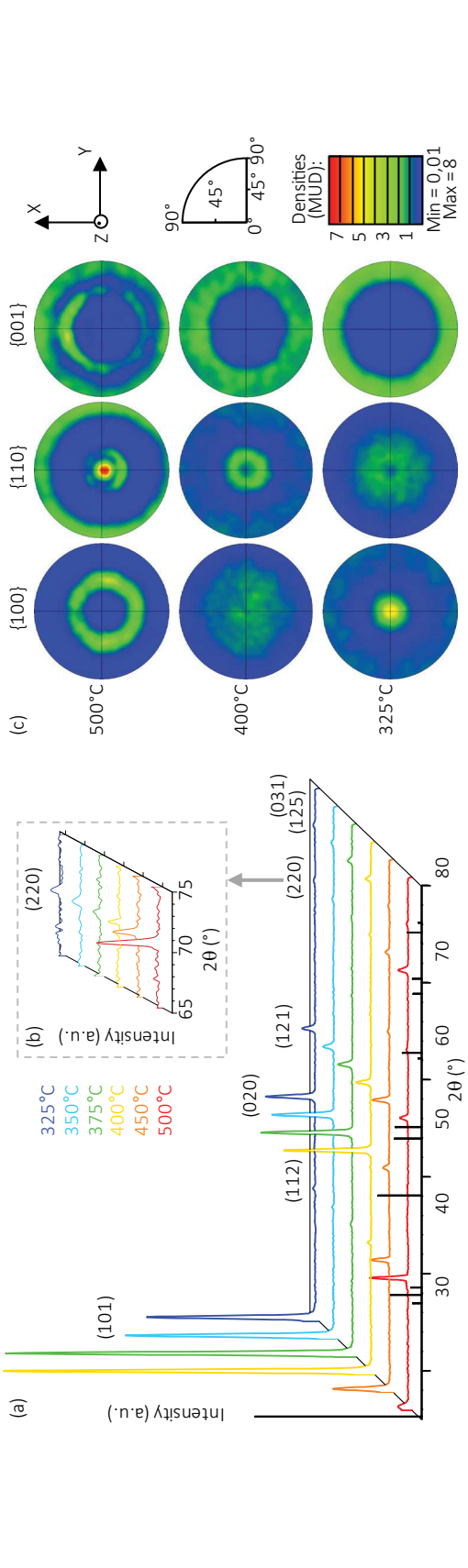

Fig. 1. (a) XRD patterns of TiO_2 films deposited on SiO_2 substrates *vs* T_d, the inset (b) presents an enlargement of the (220) peak. (c) EBSD pole figures of samples deposited at 325, 400 and 500 °C.

molecules with increasing T_d, which subsequently allows less time for entities to arrange themselves in dense structures and leads to the increase of the nucleation rate. A high T_d would favor the formation at the surface of the (112) plan, less dense than (101), and would explain the change of the texture [22]. Alternatively, the observed changes in the XRD pattern are attributed to the decrease of the c/a ratio arising from the near transition from anatase to rutile [38]. This possible initiation of change of phase and texture could explain the general decrease in intensity of the XRD pattern with increasing T_d. To further investigate the change of texture, EBSD analysis was performed on three samples deposited at 325 °C, 400 °C, and 500 °C, respectively. The EBSD pole figures are presented in Fig. 1c with the substrate surface in the XY plane. Color mapping (same color level for all maps) represents the multiples of uniform distribution (MUD), in which a high value indicates a special orientation of the corresponding crystallographic plane. The low T_d, densely structured films present a ⟨100⟩ growth direction, revealed by the MUD value of 5 in the center of the corresponding pole figure. However, if the growth was following only the ⟨100⟩ direction, it would result in an additional signal pointing at *ca.* 90° in the same pole figure, the two signals corresponding to the < 100 > and ⟨010⟩ directions, equivalent in the tetragonal system. The absence of this feature means that at least one additional texture component exists, with another growth direction whose Miller indexes are different from 0 and 1. Nevertheless, the inference that < 100 > is one of the main growth direction at low T_d, is in accordance with the evolution of the XRD patterns *vs* T_d in Fig. 1a, which show that the (020) peak (corresponding to the < 100 > direction in the tetragonal system) is the most intense at low T_d. The intermediate T_d sample (400 °C) does not present any MUD value higher than 3, indicating a transient regime with weak texture. This could be explained by a transition state between low- and high-T_d films. In contrast, the highest T_d sample (500 °C) shows a ⟨110⟩ growth direction. The corresponding most intense MUD value of 8 reveals the strongest texture among all samples. This evolution is consistent with XRD results in Fig. 1b, which show that the intensity of the (220) peak increases with increasing T_d and reaches a maximum at 500 °C. There is strong evidence of at least one more texture component in this sample. Indeed, the {110} pole figure shows not only the central disk and a circle at *ca.* 90°, both belonging to the texture component already mentioned, but also a supplementary ring at *ca.* 25°. Furthermore, the {001} pole figure shows a ring at *ca.* 50°, in addition to the ring at *ca.* 90° that belongs to the first texture component.

Fig. 2a shows the FIR-FTIR spectra of the TiO_2 films normalized by their thicknesses as a function of T_d. The FIR transmission spectra were obtained with normal incidence. The spectra present peaks at 260 and 440 cm^{-1}, which correspond to the anatase transverse optical phonons TO_1 and TO_3, respectively, as reported by González et al. [39]. Two broad shoulders centered at *ca.* 340 and 400 cm^{-1} are noticeable. The first shoulder corresponds to the TO_2 contribution. With increasing T_d, the TO_1 and TO_3 bands experience a general broadening, corresponding to the greater contribution of the previously mentioned shoulders, and an intensity decrease resulting from the increase in the porosity. Therefore, the TO_2/TO_1 intensity ratio increases.

Moreover, a third shoulder emerges at *ca.* 520 cm^{-1} at 375 °C and above. The increase of the intensity of this broad shoulder with increasing T_d is explained by the progressive increase of voids among the crystallites [29].

Fig. 2b shows MIR-FTIR spectra with an incidence angle of 70°. This configuration enables probing the longitudinal optical (LO) modes, which have a wave vector perpendicular to the film surface, in addition to the TO modes. This phenomenon, known as Berreman effect, has been highlighted by Trasferetti et al. [40] to identify the LO and TO bands of anatase, rutile, and amorphous TiO_2. In the present case, the FTIR analysis shows that the films are composed of anatase only, with two major peaks around 440 cm^{-1} (TO_3) and 855 cm^{-1} (LO_3), in agreement with XRD and Raman analysis (not shown here) that did not

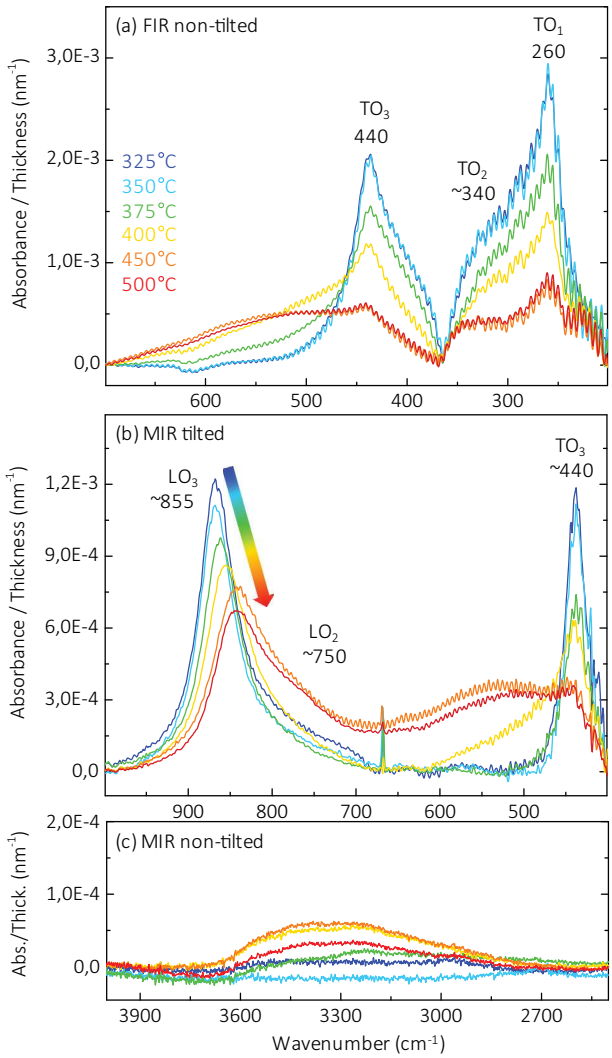

Fig. 2. FTIR spectra of films deposited at different T_d. (a) Normal incidence FIR spectra, (b) 70° tilted MIR spectra (c) Normal incidence MIR spectra.

reveal any other crystal phase. The evolution of the TO_3 peak intensity with increasing T_d remains the same as previously described for normal incidence FIR measurements. In addition, LO_3 peak intensity decreases as well, but to a lesser extent, resulting in the increase of the LO_3/TO_3 peak intensity ratio. In addition, a shoulder is observed at *ca.* 750 cm^{-1}, which can be related to the contribution of the LO_2. The evolution of the LO bands may be connected to the change in texture observed by EBSD and could suggest that high T_d samples have an orientation of the crystallites that favors the LO probe [41]. Moreover, with increasing T_d the LO_3 peak shifts progressively from 866 cm^{-1} to 842 cm^{-1}, as highlighted by the arrow, with a concomitant increase of the LO_3/TO_3 intensity ratio. This is not discussed in the literature for TiO_2; however, Primeau et al. observed a drop of the LO_3/TO_3 intensity ratio and an inherent blue-shift of the LO_3 band with an increase in the annealing temperatures of SiO_2 samples [42]. This behavior could be related to the densification of the structure and the decrease of disorder. Therefore, the observed LO_3 red-shift and the increase of the LO_3/TO_3 intensity ratio with increasing T_d can be explained by the increase in porosity and by the subsequent impact on density and disorder. Another indirect indication of the increase in the porosity is a broad and weak band in Fig. 2c, centered at *ca.* 3300 cm^{-1}, which corresponds to the stretching vibration of un-dissociated water [43,44]. The broad band intensity is globally higher for the high T_d samples, because of their highest porosity (as previously shown by the emergence of the

520 cm^{-1} contribution), which results in a higher amount of water adsorbed on the surface.

The crystallinity of the highest T_d sample was investigated by TEM as follows: the diffraction pattern of a selected area was divided in six sections and the six resulting dark field images were superimposed (Fig. S1, SI). Since bright parts are crystalline (and well oriented) in dark field images, if a dark part is crystalline on the superimposition image, then every brighter section is crystalline as well. For this reason, the area in the small black square on the figure, which is one of the darkest parts of the probed sample zone, was investigated by high resolution TEM (HRTEM). Its fast Fourier transform, also presented in Fig. S1b (SI), reveals diffraction spots corresponding to the crystallographic planes of anatase. It is thus concluded that the entire area and, consequently, the film as a whole (considering the good homogeneity of the sample), is crystalline. Fig. S2b–c (SI) shows the diffraction pattern of two encircled areas of the dense lowest T_d sample (325 °C) and Fig. S2b–c (SI) shows the summit of a grain and its crystallographic plans: both reveal that this film is entirely crystalline.

3.2. Morphology

The morphological evolution of the TiO_2 films with T_d is studied by FESEM. Fig. 3 presents top-down (left) and 25° tilted cross-sectional (right) FESEM micrographs of the TiO_2 films. With increasing T_d, both surface and cross-sectional micrographs show a decrease in the size of the various structures, with morphologies evolving from dense and angular structures to isolated and nanostructured tree-like columns. It is noticeable that the films deposited at 325 and 350 °C show similar morphologies, and the same holds for those deposited at 450 and 500 °C. The transition from compact to columnar morphology is initiated at 375 °C, as shown by the subdivision of grains on the top-down micrograph (left). The morphology evolves further at 400 °C, at which point a rather disordered columnar structure emerges. The evolution of the morphology with the increase of T_d is accompanied by a significant increase in the porosity: at 375 °C, it is manifested only between grains, whereas at 400 °C and above, it is also manifested in the small features that can be observed within the columns. Therefore, the specific surface area of the films increases considerably with increasing T_d.

Images were analyzed with the nanoTOPO_SEM™ software (Fig. 4) to achieve a quantitative description of the film morphology. Fig. 4a shows the evolution of the correlation length (CL) and the spatial periodicity, which are related to the grain size and density, with T_d. Fig. 4b shows the evolution of skewness and kurtosis, which are related to the porosity.

The CL describes distances with pixels of same grey levels on the FESEM images. Therefore, in the present case, it depends on the grain size and illustrates its evolution. With increasing T_d, CL decreases drastically from 67 nm at 325 °C to 13 nm at 375 °C, and then reaches a plateau. This behavior is attributed to the co-existence of two grain sizes in the surface morphology of films deposited between 350 and 450 °C. Since CL is calculated from the short-distance behavior of the autocorrelation function of image pixels, it is more sensitive to the smaller size: consequently, in the present case, it captures the very first appearance of the columnar structure in surface morphologies at 375 °C.

The spatial periodicity is calculated from the inverse of the spatial frequency, which corresponds to the more prominent peak of the Fourier transform of the FESEM image. For samples deposited at 325 and 350 °C, which are characterized by closely packed structures, the spatial periodicity value is *ca.* 500 nm. This evaluation of the size of the repeat unit corresponds to the width of a pack with different local elevations. Increasing T_d results in an overall decrease in the spatial periodicity. Stabilization occurs for the samples deposited at 450 and 500 °C: *ca.* 88 nm. In this case of discrete surface features, this value describes the mean distance between one side of a column and the equivalent position on the next column, including the inter-columnar

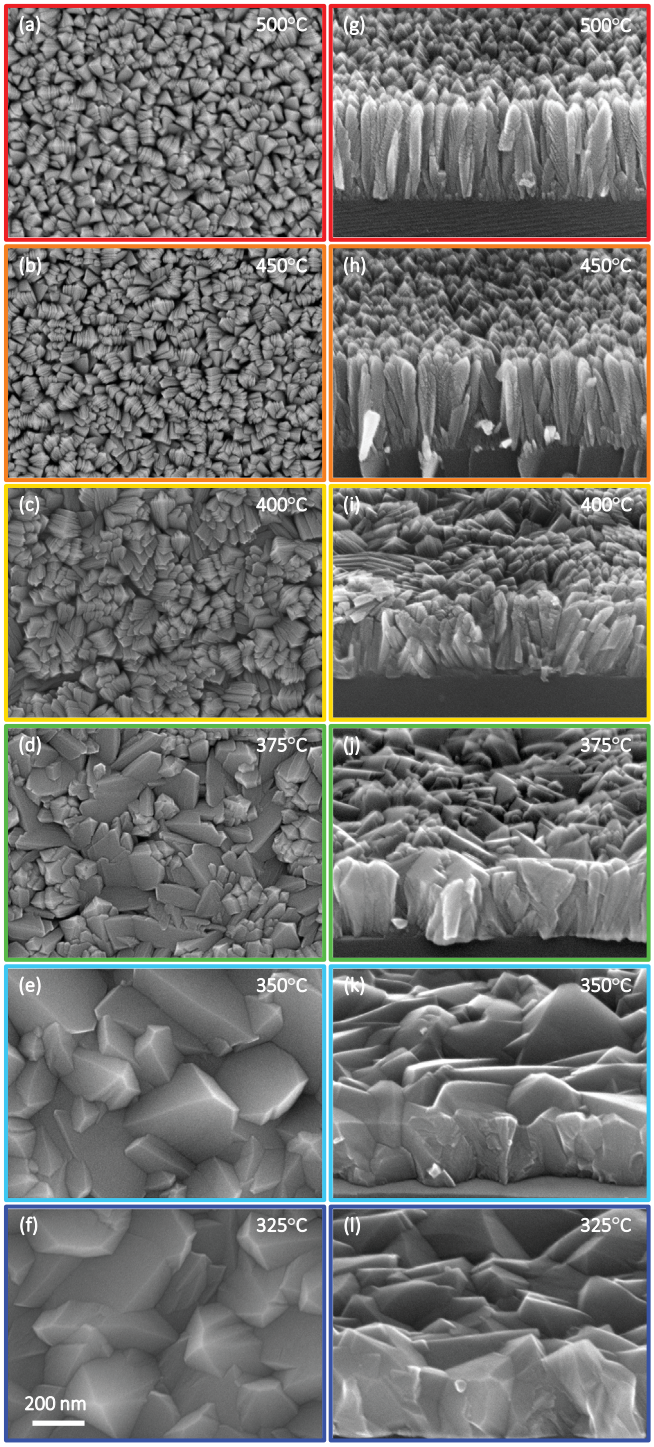

Fig. 3. FESEM images of samples deposited at different T_d, (a–f) plan-view on the left, (g–l) 25° tilted cross-sections on the right. The scale bar is the same for every images.

porosity. In contrast with CL, which already reaches a plateau at 375 °C, the spatial periodicity saturates only at the end of the morphological transition when the compact structures have been completely eliminated and the vertical columns cover the whole surface. This is due to the method of evaluating the spatial periodicity, which is sensitive to the presence of large features when mixed morphologies, composed of compact and columnar structures, co-exist. Complementary to CL, which marks the beginning of the surface morphological transition at 375 °C, the spatial periodicity is an indicator of the end of the transition

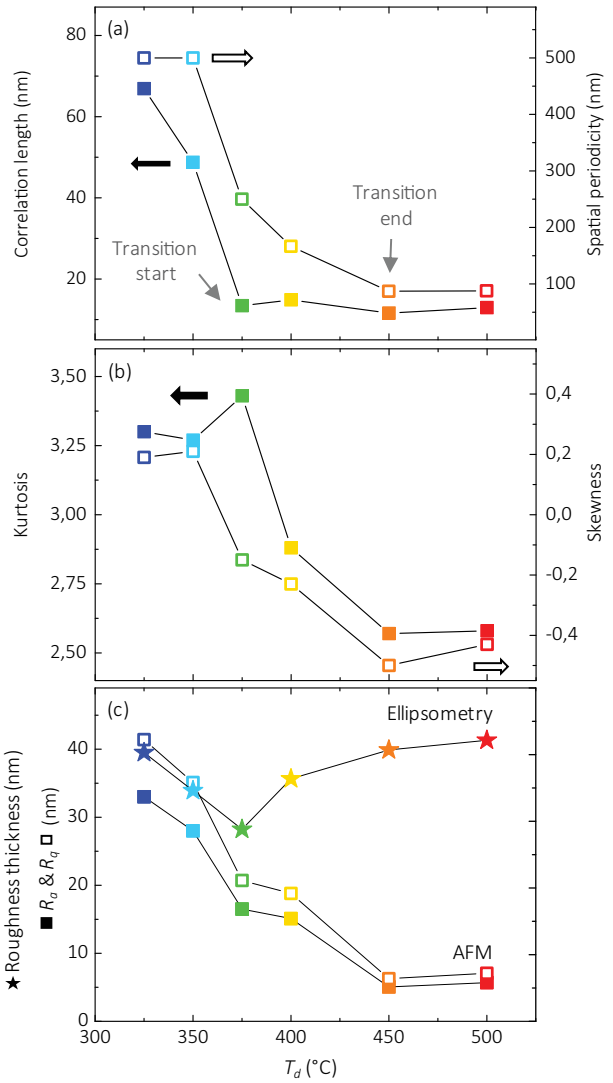

Fig. 4. FESEM images analysis parameters *vs* T_d. (a) Correlation length (CL) and spatial periodicity. (b) Kurtosis and skewness. (c) AFM R_a and R_q roughness values, and ellipsometric roughness *vs* T_d.

that occurs at 450 °C.

Skewness and kurtosis (Fig. 4b) are two parameters describing the shape of the grey level histogram of images. Kurtosis describes the flatness of the histogram, thereby discriminating the case in which there is a strong contribution of the dark and light pixels (kurtosis < 3) from the images in which the vast majority of pixels is around the mean grey level (kurtosis > 3). Kurtosis values are higher than 3 for the three samples deposited between 325 and 375 °C, corresponding to a significant contribution for these samples from mean grey pixels, and consequently to relatively flat surfaces with small local slopes. For the three samples deposited at the highest T_d, kurtosis values are lower than 3 because of the greater contribution of brighter pixels (corresponding to the extremities of columns) and darker pixels (corresponding to the porosity among columns). Skewness characterizes the symmetry of the histogram; *i.e.* whether the darker (skewness < 0) or the lighter (skewness > 0) pixels are the more prominent. It becomes negative above 375 °C, revealing the gradual darkening of the micrographs that marks, the emergence of the inter-columnar porosity.

Fig. 4c illustrates the evolution of the arithmetical mean deviation (R_a) and the root mean squared (R_q) roughness of the assessed profile with increasing T_d. The R_a and R_q of films deposited at 325 °C equal 33 and 42 nm, respectively. These values show consistent evolution, *i.e.* they monotonically decrease with increasing T_d and are stabilized at 5 nm at 450 °C and above. A complementary approach to the estimation of the roughness is provided by SE analysis, where roughness is simulated by a surface layer composed of a volume fraction of void and of TiO_2 following the Bruggeman effective medium approximation. Fig. 4c also shows the evolution of the thickness of this roughness layer *vs* T_d. The thickness is 40 nm at 325 °C, which then decreases to 28 nm at 375 °C and finally increases to reach the maximum value of 42 nm at 500 °C. Whereas the three lowest T_d samples give consistent roughness results regardless of the probing technique (photons or mechanical probe), the values for the columnar samples depend strongly on the probing method, namely on its depth sensitivity. SE analysis seems to take into account the beginning of the inter-columnar void below the summits, in contrast with the AFM tip, which cannot probe the porosity among adjacent columns at a fine scale.

To obtain a deeper insight into the morphology of the columnar 500 °C film, we compare TEM and FESEM micrographs in Fig. 5. The sample is 15° tilted in the plane of the images on all TEM images. The FESEM cross-section image, Fig. 5a, shows bottom-up oriented, cypress-like columns, illustrated by the inset scheme. The surface micrograph of Fig. 5b shows compact triangular superstructures, which are

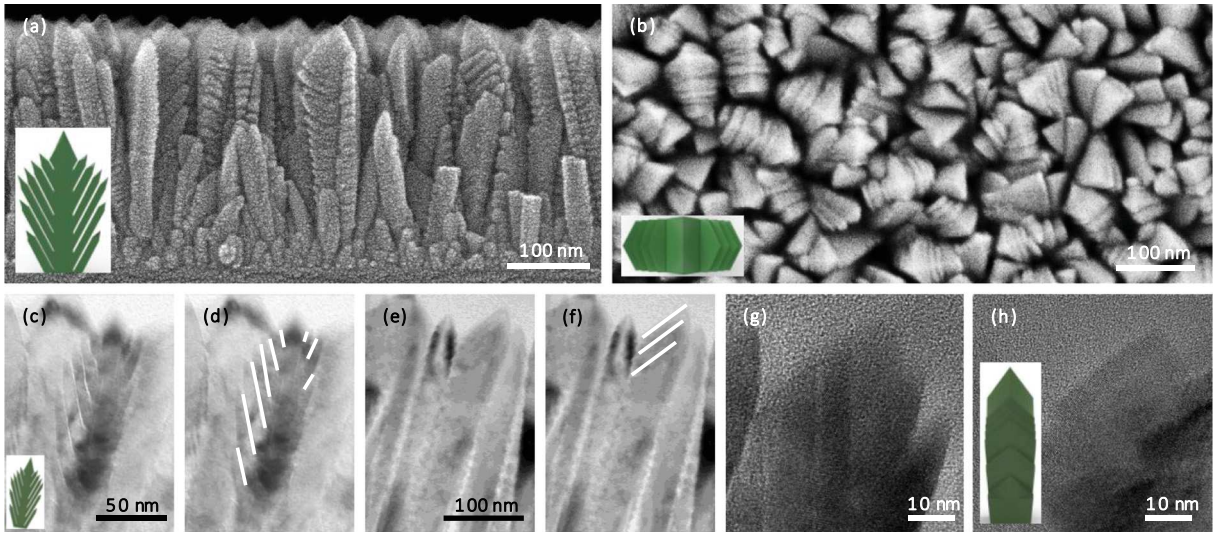

Fig. 5. Electron microscopy images of the 500 °C anatase film. (a) Cross-section FESEM image. (b) Top-view FESEM image. (c–d) Cypress-like TEM image. (e–f) Fir-like TEM image. (g) HRTEM of the cypress-like summit. (h) HRTEM of the apparent conical-shaped summit.

comparable with the top view scheme of cypress-like columns. Bottom-up oriented cypress-like columns are also visible in the TEM cross-section in Fig. 5c–d. However, in some rare cases, the layers of the structure are oriented toward the substrate, resembling a fir-like morphology as shown in Fig. 5e–f. We conclude that the layered structures present a wide range of orientations, with an apparent predominance toward the top. Fig. 5 (panels g and h) shows HRTEM micrographs of two columns, a cypress-like summit and an apparently conical one, which may represent the same structure from two different perspectives. All micrographs highlight the high specific surface of the 500 °C samples formed by such columnar morphology.

TEM analysis indicates that the column summits are monocrystalline. In contrast with the low T_d morphology composed of monolithic grains, this 500 °C film morphology composed of a forest of tree-like nanostructures is far more complex. It exhibits small-scale details and large variability in the orientation of the films. Therefore, taking into account the different sides of each column and column layer, this implies that the columnar structure exhibits a higher diversity in the crystallographic facets at the surface than the dense films.

3.3. Mechanical characteristics

Fig. 6a–c presents the AFM surface micrographs of the 325, 375 and 450 °C samples. The observed morphology is in agreement with the FESEM images. Deformation maps of the same probed sample area for a maximum applied force of 65 nN are shown in Fig. 6d–f. Fig. 6g is the deformation occurrence diagram of the six samples. The dense 325 °C film exhibits a mechanical response to stress that differs from one grain facet to another, resulting in the observation of six main different deformation areas (see the blue arrows). For intermediate T_d, three different deformation areas remain, whereas at higher T_d (450 °C and 500 °C) the deformation is homogenous over the surface. At low T_d, the diversity in mechanical responses is probably linked to small variations in the Young's modulus as a function of crystallographic orientation [45]. At high T_d, we link the decrease in the diversity of deformation areas to the general decrease in the grain size, which means that what is probed at higher T_d is the mechanical response of a group of nanostructured tree-like columns with different crystallographic planes. It is also noticeable that the mean deformation under a fixed applied force increases globally with T_d, *i.e.* with the change in morphology from dense to columnar. This is compatible with the increase in the porosity within and between the grain, which enables easier deformation.

The residual stress of the films was investigated by GIXRD. For all samples, the residual stresses are compressive and increase from -150 ± 20 MPa at 325 °C to -300 ± 100 MPa at 450 °C, as shown in the inset of Fig. 6g. These values are low compared to the Young's modulus of bulk (195 GPa [45]) and the stress of anatase films reported in the literature for different deposition techniques (sol-gel: -2185 MPa [46], sputtering: -890 MPa [26], ALD: -700 MPa [45]). As mentioned in Section 2 of the SI, these anatase films are supposed to be quasi-isotropic and two stress origins can be considered: σ_g, the film growth stress induced during the deposition and σ_{th}, the thermal stress induced by the difference in the thermal expansion coefficients of the SiO_2 substrate and the TiO_2 film during cooling after deposition. The residual stress can be a mixture of thermal and growth stress. For the films deposited, the estimates of thermal stress σ_{th} in the film range between 798 and 1256 MPa, as shown in Section 2 in SI. Therefore, excluding the thermal stress, the growth stress for all the samples is strongly compressive, ranging between -948 and -1425 MPa. This compressive growth stress is very likely to ensue from the evolution of

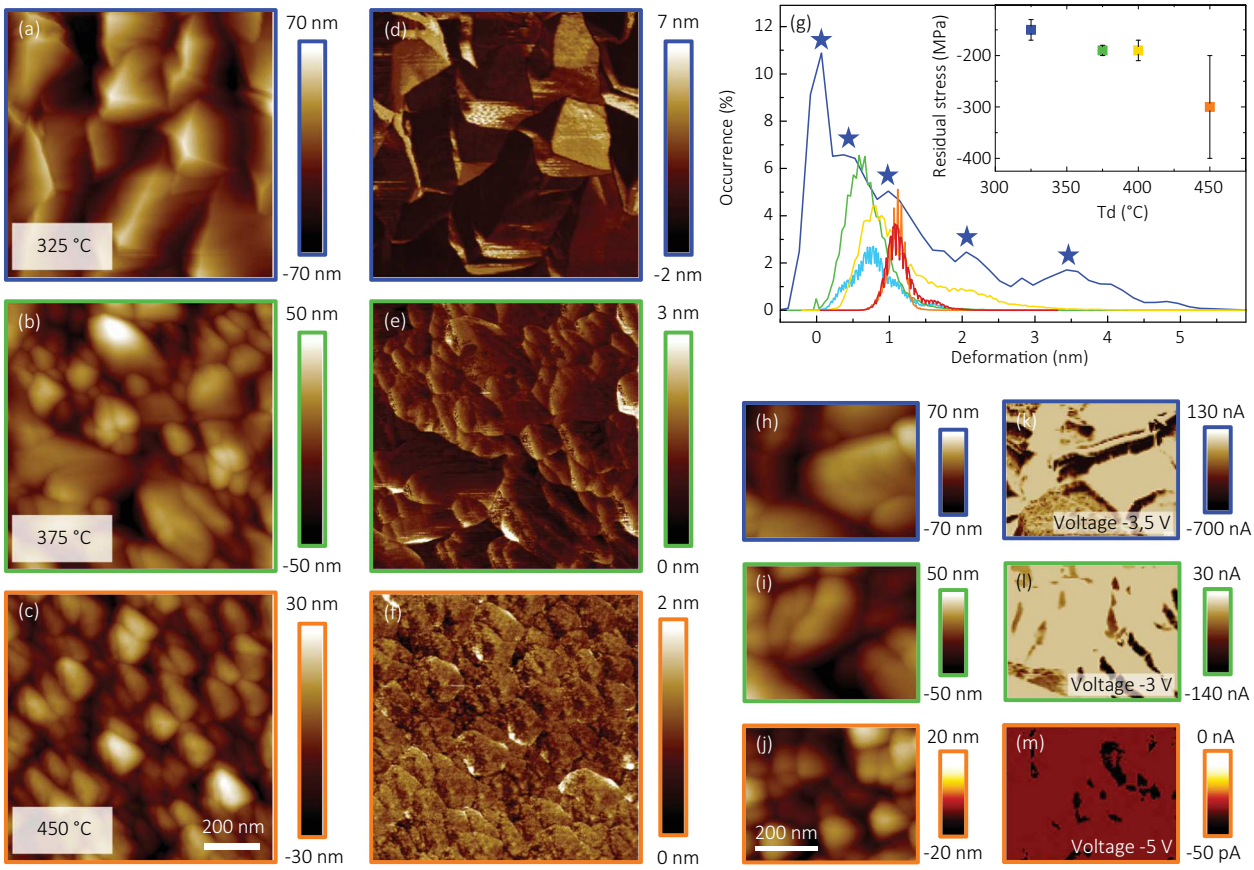

Fig. 6. (a–c) Evolution of topography and (d–f) deformation for three different T_d, 325 °C (a, d), 375 °C (b, e) and 450 °C (c, f). (g) Mechanical aspects: influence of T_d on deformation occurrence, the insert shows the residual stress σ against T_d probed by GIXRD. (h–j) Topographic maps corresponding to the current maps: (h) 325 °C, (i) 375 °C and (j) 450 °C.

the morphology and texture.

3.4. Electrical characteristics

Fig. 6h–j shows the current maps of the TiO_2 samples deposited at 325, 375, and 450 °C, probed under negative voltage. The maps show a decrease in the maximum current (see the current scale on the right) with the increase of T_d. However, these maximum values are related to very small areas of the maps. Therefore, the mean values are more representative of the evolution of the electrical properties of the films. Under the same applied voltage of -3 V, they are −108, −6, and 0 nA for samples deposited at 325, 375, and 450 °C, respectively. They take into account the conductive area ratios, which are 50, 14, and 10%, respectively. The general decrease in charge transport with the increase in T_d follows the appearance of the columnar structures and of the increase in the porosity.

Hall effect measurements on samples deposited at 325 and 400 °C evidence the n-type character of the TiO_2 films. It is reasonable to assume that the samples deposited at intermediate T_d, *i.e.* 350 and 375 °C, are n-type semiconductors as well. Furthermore, charge carrier density for the 325 °C sample is $1 \pm 0.3 \times 10^{18}\ cm^{-3}$ and that for the sample deposited at 400 °C is $2.9 \pm 0.2 \times 10^{18}\ cm^{-3}$. This increase implies a decrease in the charge mobility, which can be attributed to the increased complexity of the morphology with the emergence of voids between and inside the nanostructures.

3.5. Optical characterization

In order to determine the optical band-gap *Eg* of the films, we plot in Fig. 7a the Tauc plot of the absorption coefficient α for indirect semiconductors. Despite the fact that all films present similar thicknesses determined by SE and by FESEM (295–435 nm), it is clear that interference fringes below the optical absorption edge disappear for low T_d films (< 400 °C). This is because of light scattering caused by larger nanostructures above 300 nm that clearly emerge below 400 °C, as shown by FESEM and AFM (Fig. 3 and Fig. 6a–c). This is confirmed by the diffuse reflectance spectra showing a significant increase in intensity while T_d decreases to below 400 °C (Fig. S3a, SI). In addition, we also analyze the optical properties below the band-gap by SE using the exponential Urbach formalism of the Cody-Lorenz model *i.e.* the slope *Eu* and the demarcation energy E_t between the Urbach tail transition and the band edge [47]. The evolution of *Eu* with T_d (Fig. S4, SI) is the inverse of the evolution of the reflected diffuse light intensity. Therefore, we can conclude that the loss of light in the transparent spectral domain is probably because of scattering and not because of Urbach states. Moreover, scattering seems to be the main cause of the reflection, since the total (Fig. S3b Si) and diffuse (Fig. S3b.a SI) reflectance spectra are very similar in the UV range. At 285 nm, both spectra show a major increase with decreasing T_d, from 8 to 27% and 0.5 to 25% respectively. This means that at low T_d, up to 25% of the intensity of light is lost for the photocatalytic process because of scattering.

The insert of Fig. 7a shows that *Eg* determined by transmission spectroscopy decreases monotonously from 3.25 at 500 °C, which corresponds to bulk anatase, to 2.94 at 375 °C. Despite the difficulty of determining the optical band edge from the linear part of the Tauc plot because of interferences and scattering, this monotonous trend is similar to the one estimated by SE on the entire series (see Fig. 7a). A slight shift is observed between the two measurements, which has already been observed with various Si alloys and may be inherent to the Cody-Lorentz model [47].

The decrease of *Eg* with decreasing T_d could result from the progressive increase of the content of shallow donor levels caused by intrinsic defects as oxygen's vacancies (O_v) and/or Ti^{3+} oxidation states. Valence band spectra from XPS measurements of samples deposited at 325 and 450 °C are similar, as shown in Fig. S5a (SI), which would point to an apparent downshift of the conduction band of low T_d samples. However, we do not detect any distinctive signatures of Ti^{3+} or O_v in surface XPS spectra (Fig. S5b, c–h, SI). Indeed, the 531.8 eV contribution can be related to oxygen from adsorbed carbon species or OH groups, as well as O_v [48]. Also, depth analysis with argon cluster sputtering would induce a reduction effect that would bias the results. Moreover, Hall effect measurements show an increase in the concentration of charge carriers with the increase of T_d. Therefore, the decrease in the optical absorption threshold with decreasing T_d could be partly related to the progressive increase of scattering (Fig. S3, SI). Nevertheless, the SE band-gap also decreases with T_d despite the use of an Urbach tail contribution for the deconvolution of the scattering. This suggests that the band-gap may be narrowed with decreasing T_d.

Fig. 7b shows the ellipsometric angles Ψ and Δ of the sample deposited at 350 °C, and the simulated SE data using the film architecture displayed in the inset of Fig. 7c. It is worth noting the high fit quality in the transparent region and above the absorption edge. Furthermore, the refractive index *n* and the extinction coefficient *k* reported in Fig. S6 (SI) using the Cody-Lorentz model are similar to previous SE spectra used to analyze amorphous and crystalline anatase [32,49,50]. We observed an increase in *n* with decreasing T_d (Fig. S6, SI). This increase of *n* is caused by the rise in the density. Thus, the rise of the optical reflection (Fig. S3b Si), which is mainly due to scattering, is explained by the concomitant increase of the size of the nanostructures and the refractive index.

Fig. 7c shows the volume fractions of void (f_{void}) *vs* T_d estimated from *n*@633 nm of the films, and of bulk anatase following the Lorentz-Lorenz equation. In this case, f_{void} is an estimate of the total porosity, including the closed porosity, whereas the volume fraction of ethanol resulting from SEP corresponds only to the open mesoporosity with a maximum pore size of *ca.* 20 nm. We attribute the difference between the results to the fact that the large mesoporosity and macroporosity cannot be filled by ethanol by capillary condensation. The closed

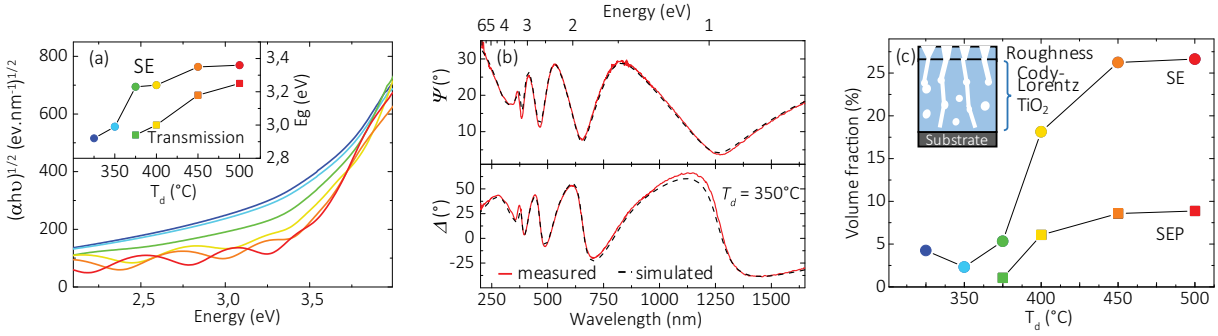

Fig. 7. (a) Tauc plot of the absorption coefficient determined by UV–Vis-Nir transmission spectroscopy for samples deposited at the different T_d – the inset shows films E_g determined by UV–vis-Nir transmission spectroscopy and by SE. (b) Ellipsometric angles Ψ and Δ of the TiO_2 thin film deposited at 350 °C. (c) Porosity volume fraction from SE and SEP - the inset describes the structure used to determine the ellipsometric model.

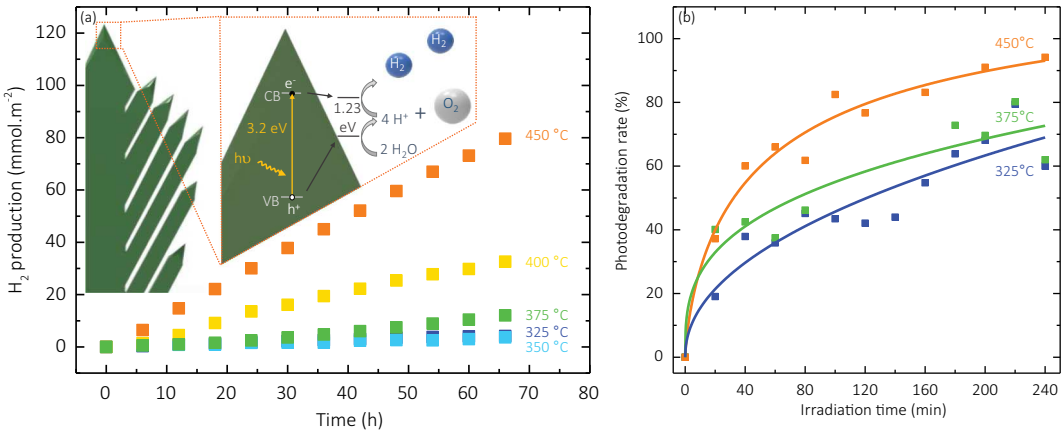

Fig. 8. Photocatalytic evaluation of samples deposited at different T_d, (a) H_2 photogeneration, (b) Pilkington test.

porosity, inaccessible to ethanol, could be negligible in the porous structure. No model using effective medium approximations composed of void and crystalline and/or amorphous anatase could significantly fit the SE data, since it cannot accurately describe band-gap and scattering intensity variations. Therefore, the values reported in Fig. 7c inset *vs* T_d are only indicative. However, the increase of both volume fractions with increasing T_d reflects the increase in porosity within and between the nanostructures, which is apparent in the FESEM and HRTEM images (Fig. 5).

3.6. Photocatalytic evaluation

To study the evolution of the SWS photocatalytic properties of the TiO_2 films *vs* T_d, two tests were carried out. First, water photodissociation rates are quantified by the cumulative H_2 production. Fig. 8a shows the amounts of H_2 as a function of time produced by photocatalysis by the films deposited between 450 and 325 °C, corresponding to the entire range of morphologies. All films display constant H_2 production throughout the 66 h of the analysis, as shown by the linearity of the curves, revealing their high stability. Furthermore, the repeatability of the experiments has been established by testing a 450 °C sample thrice and acquiring the same results. After 66 h, the well-organized, nanotree-shaped TiO_2 (450 °C) displays the highest cumulative H_2 production of 78.9 mmol.m^{-2}. After the same duration, the TiO_2 with disorganized columns (400 °C) shows a production of only 36.2 mmol.m^{-2}, *i.e.* less than half of the production of the film deposited at 450 °C. The intermediate, 375 °C sample displays a production of 12 mmol.m^{-2} and the two dense TiO_2 show similar production quantities of 3.6 and 4.4 mmol.m^{-2} for 350 and 325 °C, respectively. The well organized columnar film shows the best photocatalytic performance, which is far better than the others. Comparison of these results with the literature is difficult because of the diversity of the reported photocatalytic protocols used, in terms of solutions, protocol pressure, normalization, or intensity of the light source [51].

A second photocatalytic analysis was performed by the Pilkington test, shown in Fig. 8b, following the photodegradation of stearic acid under UV-light illumination. The results of three samples (325, 375 and 450 °C) exhibiting the three characteristic morphologies are shown, revealing that the photocatalytic activity of the high T_d sample is better than the 375 and the 325 °C ones. The highest photodegradation rate is close to the rate from PECVD-processed pure anatase TiO_2 film reported by Zhou et al [34].

The straight hierarchy between the photodegradation rates of the three samples shown on the Fig. 8b can be attenuated by the other samples results (Fig. S7, SI) that show, for instance, that the 400 °C sample is more efficient than the 450 °C sample. Additional results on Fig. S7 (SI) also show that initially, the sample deposited at 350 °C is more active than the one deposited at 325 °C.

Both analyses show the strong tendency of higher T_d samples to show higher photocatalytic activity. For H_2 photogeneration, there is only one small exception to this trend – the samples deposited at 325 and 350 °C – since the former exhibits slightly better activity than the latter. However, as described earlier, several samples do not follow the trend for stearic acid photodegradation. These exceptions are not surprising when one considers the fact that competition among a number of properties and characteristics results in the final photocatalytic performance of the materials. This is especially the case given that the properties do not show a steady evolution with T_d. For instance, this is the case with the mean current probed by C-AFM, which shows a strong early decrease with the increase of T_d, or for the evolution of XRD patterns, in which significant change begins only at 450 °C. Moreover, the evolution of some properties is not quite monotonous: for example, the porosity as determined by ellipsometry between 325 and 350 °C. Finally, the initial amount of stearic acid on surface samples could be different from one sample to another because of specific surface differences between them, which could explain the fact that stearic acid photodegradation results show more exceptions to the general trend. Therefore, the 400 °C sample, which is less porous than the 450 °C one, could have less acid stearic to photodegrade in the first place. For all these reasons, we focus in the following discussion on only the general trend, which is indisputable.

4. Discussion

The strong increase in the morphological complexity of anatase films obtained with increasing T_d has a positive impact on the photocatalytic performance. This impact can be analyzed by the following photocatalytic mechanisms: carrier photogeneration, carrier concentration, carrier transport, and properties of the surfaces exposed to the aqueous catalytic solutions. Changes in the morphology of TiO_2 films with increasing T_d have been reported extensively in the literature. Taylor et al. [21] observed the same morphological evolution of MOCVD TiO_2 films from TTIP. According to them, the increase of T_d results in the decrease in the migration length of active species and in a concomitant decrease in the number of hops before reaction. Therefore, at low T_d, reactive species have time to diffuse, which results in large and compact structures, whereas high T_d favors nucleation and leads to preferential growth on pre-existing structures. This, in turn, leads to the formation of the columnar complex nanotrees, which GIXRD reveals to be compressed, and more subject to deformation under fixed applied force. This growth mechanism leads to highly porous films at high T_d, estimated to be *ca.* 26 vol% of void by SE. Further evidence is provided by FTIR, which shows a significant decrease in the number of Ti—O

TO_{1-3} vibrations with increasing T_d, by the concomitant drop in the TO_3/LO_3 intensity ratio, which is also an indication of increasing disorder, and by the LO_3 red-shift. The high porosity generated by the nanotree structuration is mainly in the form of space between columns, as revealed by the analysis of the plan-view FESEM images and shown by the inter-columnar gaps in the cross-sectional FESEM and HRTEM images. This nanostructuration leads to nanotree morphologies, the most common of which exhibits branches directed toward the top, resembling a cypress. The conical shaped summits seem to belong to the same morphology but observed from a different side. This results in a high specific surface which is also evidenced by the appearance of the 520 cm^{-1} FTIR contribution. The change in the morphology of the TiO_2 films with increasing T_d also results in a stronger crystallographic texture and in a change in the growth direction after a transitional step, as evidenced by EBSD, and potentially by FTIR [41]. Besides, HRTEM suggests that the diversity and the number of the crystallographic facets exposed to the contact with the aqueous solutions for H_2 photogeneration or with stearic acid for the Pilkington test increase significantly with increasing T_d. Murakami et al. suggested that a balanced ratio between (101) and (001) surfaces would improve the photocatalytic performance by improving charge separation and, therefore, the lifetime of the excitons, because of the presence of both oxidative and reductive surfaces [52]. Such surfaces were confirmed by the work of Yu et al. [53], and the oxidative character of particularly the (100) surface was confirmed by Roy et al. [54]. Nevertheless, these studies concern free nanocrystallites and not films composed of dense or porous structures, where charge carrier transport plays a more significant role in the photocatalytic properties. We observed that charge carrier transport decreases significantly with the strong nanostructuration of the morphology, and the decrease in grain size, as revealed by both C-AFM and Hall effect measurements. This is consistent with the work of Chen et al., who showed that the charge mobility of small anatase nanorods (0.57 $cm^2 V^{-1} s^{-1}$) [55] is much lower than that of large crystallites (20 $cm^2 V^{-1} s^{-1}$) [9]. Further, we suspect that a larger number of grain boundaries in the nanotree TiO_2, which act as diffusion centers [56], and a higher disorder may cause charge carrier traps and ohmic behavior. Finally, the intensity of reflected light increases with increasing T_d mainly because of scattering.

We witness here the competition among different effects involved in the photocatalytic performance of the TiO_2 films with increasing T_d. The beneficial effects include the drop in the optical reflection, the increase in charge density, the huge enhancement of the exchange surface, and the higher diversity of the crystallographic facets. These effects overcome the detrimental effects, which include, potentially, the compressive residual stress [26,30], and the decrease in charge carrier mobility. The latter effect may indicate that the redox reactions mainly involve excitons generated at the extreme TiO_2 surface. As for the effect of the potential narrowing of the optical band-gap, that could hinder the photocatalytic activity by decreasing the number of absorbed photons. However, the narrowing could also be beneficial: if this downshift is strong enough to position the conduction band below the H^+/H_2 redox potential, the reduction reaction would be compromised. By contrast, high T_d samples would benefit from the thermodynamic driving force arising from a suitable position of the conduction band [57], as shown in Fig. 8a.

5. Conclusion

We deposited anatase TiO_2 films by thermal MOCVD. In this process, increasing T_d induces a strong increase in morphological complexity through the formation of nanotree-like columnar structures. The positive impact of this change on the water-splitting performance is investigated. We observe a 66 h cumulative H_2 production that increases from 4.4 to 78.9 $mmol.m^{-2}$ as T_d increases from 325 to 450 °C. In the complex competition between the numerous properties affecting the photocatalytic mechanisms, we attribute the better activity of the high T_d samples to the strong increase in the specific surface area. This increase is induced by spaces between the nanotree-like columnar structures and possibly by the smaller space within each column, which were observed by both FESEM and HRTEM, in accordance with FTIR analyses. We also observe a significant increase in the porosity with increasing T_d. The maximum volume fractions of void corresponding to the open mesoporosity (estimated by SEP) and full porosity (estimated by SE) were 9% and 26%, respectively. Moreover, we observe a decrease in the optical reflection with increasing T_d, which is mainly caused by scattering and which may favor the photocatalytic process. In addition, the inherent increase in the diversity of the exposed crystallographic facets with the increase in the morphological complexity may have a positive impact on the H_2 production performance as well. Notably, we show for the first time by EBSD a change of one of the main growth direction: < 100 > at 325 °C and < 110 > at 500 °C. However, we observe a decrease of the charge mobility, which is detrimental to the photocatalytic performance, as could be the case with the increase in the residual compressive stress. Therefore, we have performed an extended investigation of the nanoscale electrical and electronic properties with regard to the crystallographic properties of the nanotree-shaped TiO_2. The results of this analysis will be published in a forthcoming paper.

Acknowledgements

This work was supported by funding from Toulouse Tech'Interlab and Association Instituts Carnot. The photocatalytic experiments were supported by the Université de Toulouse (IDEX MUSE).

We are indebted to Claire Tendero, Diane Samelor, Daniel Sadowski, Cédric Charvillat, Olivier Marsan, Jérôme Esvan, Benoît Malard, Bertrand Viguier, Alessandro Pugliara (Cirimat), Stéphane Leblond du Plouy, Arnaud Proietti, Claudie Josse (UMS Castaing) and Emmanouil Soulos (IEM) for their contributions to this work.

Appendix A. Supplementary data

Supplementary data to this article can be found online at https://doi.org/10.1016/j.apsusc.2019.07.191.

References

[1] J. Yu, Z. Chen, L. Zeng, Y. Ma, Z. Feng, Y. Wu, H. Lin, L. Zhao, Y. He, Synthesis of carbon-doped $KNbO_3$ photocatalyst with excellent performance for photocatalytic hydrogen production, Sol. Energy Mater. Sol. Cells 179 (2018) 45–56, https://doi.org/10.1016/j.solmat.2018.01.043.

[2] W. Michael G., W. Emily L., M. James R., B. Shannon W., M. Qixi, S. Elizabeth A., L. Nathan S., Solar water splitting cells, Chem. Rev. 110 (2010) 6446–6473. doi:https://doi.org/10.1021/cr1002326.

[3] A. Fujishima, K. Honda, Electrochemical photolysis of water at a semiconductor electrode, Nature 238 (1972) 37–38, https://doi.org/10.1038/238037a0.

[4] S.P. Krumdieck, R. Boichot, R. Gorthy, J.G. Land, S. Lay, A.J. Gardecka, M.I.J. Polson, A. Wasa, J.E. Aitken, J.A. Heinemann, G. Renou, G. Berthomé, F. Charlot, T. Encinas, M. Braccini, C.M. Bishop, Nanostructured TiO_2 anatase-rutile-carbon solid coating with visible light antimicrobial activity, Sci. Rep. 9 (2019) 1883–1893, https://doi.org/10.1038/s41598-018-38291-y.

[5] S.G. Kumar, K.S.R.K. Rao, Comparison of modification strategies towards enhanced charge carrier separation and photocatalytic degradation activity of metal oxide semiconductors (TiO_2, WO_3 and ZnO), Appl. Surf. Sci. 391 ((2017) 124–148, https://doi.org/10.1016/j.apsusc.2016.07.081.

[6] T. Sharifi, Y. Ghayeb, T. Mohammadi, M.M. Momeni, Enhanced photoelectrochemical water splitting of $CrTiO_2$ nanotube photoanodes by the decoration of their surface via the photodeposition of Ag and Au, Dalton Trans. 47 (2018) 11593–11604, https://doi.org/10.1039/c8dt02383b.

[7] M.M. Momeni, Y. Ghayeb, M. Shafiei, Preparation and characterization of $CrFeWTiO_2$ photoanodes and their photoelectrochemical activities for water splitting, Dalton Trans. 46 (2017) 12527–12536, https://doi.org/10.1039/c7dt01596h.

[8] M.M. Momeni, M. Mahvari, Y. Ghayeb, Photoelectrochemical properties of iron-cobalt $WTiO_2$ nanotube photoanodes for water splitting and photocathodic protection of stainless steel, J. Electroanal. Chem. 832 (2019) 7–23, https://doi.org/10.1016/j.jelechem.2018.10.035.

[9] H. Tang, K. Prasad, R. Sanjinès, P.E. Schmid, F. Lévy, Electrical and optical properties of TiO_2 anatase thin films, J. Appl. Phys. 75 (1994) 2042–2047, https://doi.org/10.1063/1.356306.

[10] T. Luttrell, S. Halpegamage, J. Tao, A. Kramer, E. Sutter, M. Batzill, Why is anatase a better photocatalyst than rutile? - model studies on epitaxial TiO_2 films, Sci. Rep. 4 (2015) 4043–4050. doi:https://doi.org/10.1038/srep04043.X.

[11] J. Li, N. Wu, Semiconductor-based photocatalysts and photoelectrochemical cells for solar fuel generation: a review, Catal. Sci. Technol. 5 (2015) 1360–1384, https://doi.org/10.1039/C4CY00974F.

[12] A. Kudo, Y. Miseki, Heterogeneous photocatalyst materials for water splitting, Chem. Soc. Rev. 38 (2009) 253–278, https://doi.org/10.1039/B800489G.

[13] P. Alphonse, A. Varghese, C. Tendero, Stable hydrosols for TiO_2 coatings, J. Sol-Gel Sci. Technol. 56 (2010) 250–263, https://doi.org/10.1007/s10971-010-2301-y.

[14] J. Pouilleau, D. Devilliers, F. Garrido, S. Durand-Vidal, E. Mahé, Structure and composition of passive titanium oxide films, Mater. Sci. Eng. B 47 (1997) 235–243, https://doi.org/10.1016/S0921-5107(97)00043-3.

[15] S. Nezar, N. Saoula, S. Sali, M. Faiz, M. Mekki, N.A. Laoufi, N. Tabet, Properties of TiO_2 thin films deposited by rf reactive magnetron sputtering on biased substrates, Appl. Surf. Sci. 395 (2017) 172–179, https://doi.org/10.1016/j.apsusc.2016.08.125.

[16] S.A. Gudkova, A.A. Sigarev, A.P. Alekhin, V.F. Toknova, A.S. Mitiaev, A.M. Markeev, Structural properties of the titanium dioxide thin films grown by atomic layer deposition at various numbers of reaction cycles, Appl. Surf. Sci. 257 (2010) 186–191, https://doi.org/10.1016/j.apsusc.2010.06.061.

[17] S.J. Kim, V.S. Dang, K. Xu, D. Barreca, C. Maccato, G. Carraro, R.K. Bhakta, M. Winter, H.W. Becker, D. Rogalla, C. Sada, R.A. Fischer, A. Devi, MOCVD of TiO2 thin films from a modified titanium alkoxide precursor, Phys. Status Solidi A. 212 (2015) 1563–1570, https://doi.org/10.1002/pssa.201532271.

[18] M. Baryshnikova, L. Filatov, M. Mishin, A. Uvarov, A. Kondrateva, S. Alexandrov, Evolution of the microstructure in titanium dioxide films during chemical vapor deposition, Phys. Status Solidi 212 (2015) 1533–1538, https://doi.org/10.1002/pssa.201532300.

[19] J. Park, E. Kettleson, W.-J. An, Y. Tang, P. Biswas, Inactivation of E. coli in water using photocatalytic, nanostructured films synthesized by aerosol routes, Catalysts 3 (2013) 247–260, https://doi.org/10.3390/catal3010247.

[20] D. Duminica, Fonctionnalisation de surfaces d'aciers par des procédés CVD compatibles avec le traitement de plaques au défilé : dépôts de TiO_2 et Fe, Degree thesis University of Toulouse, 2004.

[21] C.J. Taylor, D.C. Gilmer, D.G. Colombo, G.D. Wilk, S.A. Campbell, J. Roberts, W.L. Gladfelter, Does chemistry really matter in the chemical vapor deposition of titanium dioxide? Precursor and kinetic effects on the microstructure of polycrystalline films, J. Am. Chem. Soc. 121 (1999) 5220–5229, https://doi.org/10.1021/ja984446f.

[22] Z.S. Khalifa, Effect of deposition temperature on the properties of TiO_2 thin films deposited by MOCVD, Surf. Rev. Lett. 23 (2016) 1650001–1650009, https://doi.org/10.1142/S0218625X16500013.

[23] I. Paramasivam, H. Jha, N. Liu, P. Schmuki, A review of photocatalysis using self-organized TiO_2 nanotubes and other ordered oxide nanostructures, Small 8 (2012) 3073–3103, https://doi.org/10.1002/smll.201200564.

[24] F.A. Cataño, H. Gomez, E.A. Dalchiele, R.E. Marotti, Morphological and structural control of electrodeposited ZnO thin films and its influence on the photocatalytic degradation of methyl orange dye, Int. J. Electrochem. Sci. 9 (2014) 534–548, https://doi.org/10.1016/j.lungcan.2018.07.012.

[25] D. Zywitzki, H. Jing, H. Tüysüz, C.K. Chan, High surface area, amorphous titania with reactive Ti^{3+} through a photo-assisted synthesis method for photocatalytic H_2 generation, J. Mater. Chem. A 5 (2017) 10957–10967, https://doi.org/10.1039/C7TA01614J.

[26] T. Shibata, H. Irie, D.A. Tryk, K. Hashimoto, Effect of residual stress on the photochemical properties of TiO_2 thin films, J. Phys. Chem. C 113 (2009) 12811–12817, https://doi.org/10.1021/jp904037t.

[27] S. Selçuk, A. Selloni, Excess electrons at anatase TiO_2 surfaces and interfaces: insights from first principles simulations, J. Phys. D. Appl. Phys. 50 (2017) 273002–273013, https://doi.org/10.1088/1361-6463/aa7540.

[28] L. Youssef, A.J. Kinfack Leoga, S. Roualdes, J. Bassil, M. Zakhour, V. Rouessac, A. Ayral, M. Nakhl, Optimization of N-doped TiO_2 multifunctional thin layers by low frequency PECVD process, J. Eur. Ceram. Soc. 37 (2017) 5289–5303, https://doi.org/10.1016/j.jeurceramsoc.2017.05.010.

[29] M. Ocaña, C. Pecharromán, F. Gracía, J.P. Holgado, A.R. González-Elipe, Analysis of texture and microstructure of anatase thin films by Fourier transform infrared spectroscopy, Thin Solid Films 515 (2006) 1585–1591, https://doi.org/10.1016/j.tsf.2006.05.022.

[30] A. Miyamura, K. Kaneda, Y. Sato, Y. Shigesato, Effects of internal stress on photocatalytic properties of TiO_2 films, Thin Solid Films 516 (2008) 4603–4608, https://doi.org/10.1016/j.tsf.2007.05.079.

[31] Z.S. Khalifa, S.A. Mahmoud, Photocatalytic and optical properties of titanium dioxide thin films prepared by metalorganic chemical vapor deposition, Phys. E Low-Dimensional Syst. Nanostruct. 91 (2017) 60–64, https://doi.org/10.1016/j.physe.2017.03.010.

[32] M. Horprathum, P. Chindaudom, P. Limnonthakul, P. Eiamchai, N. Nuntawong, V. Patthanasettakul, A. Pokaipisit, P. Limsuwan, Fabrication and characterization of hydrophilic TiO_2 thin films on unheated substrates prepared by pulsed DC reactive magnetron sputtering, J. Nanomater. 2010 (2010) 1–7, https://doi.org/10.1155/2010/841659.

[33] A. Mills, J. Wang, Simultaneous monitoring of the destruction of stearic acid and generation of carbon dioxide by self-cleaning semiconductor photocatalytic films, J. Photochem. Photobiol. A Chem. 182 (2006) 181–186, https://doi.org/10.1016/j.jphotochem.2006.02.010.

[34] M. Zhou, S. Roualdès, A. Ayral, New photocatalytic contactors obtained by PECVD deposition of TiO_2 thin layers on the surface of macroporous supports: PECVD TiO_2-based membranes as photocatalytic contactors, Eur. Phys. J. Spec. Top. 224 (2015) 1871–1882, https://doi.org/10.1140/epjst/e2015-02506-8.

[35] M.N. Ghazzal, N. Barthen, N. Chaoui, Photodegradation kinetics of stearic acid on UV-irradiated titania thin film separately followed by optical microscopy and Fourier transform infrared spectroscopy, Appl. Catal. B Environ. 103 (2011) 85–90, https://doi.org/10.1016/j.apcatb.2011.01.013.

[36] M.C. Vebber, A.C.R. Faria, N. Dal'Acqua, L.L. Beal, G. Fetter, G. Machado, M. Giovanela, J.S. Crespo, Hydrogen production by photocatalytic water splitting using poly(allylamine hydrochloride)/poly(acrylic acid)/TiO_2/copper chlorophyllin self-assembled thin films, Int. J. Hydrog. Energy 41 (2016) 17995–18004, https://doi.org/10.1016/j.ijhydene.2016.07.238.

[37] I.G. Aviziotis, N. Cheimarios, T. Duguet, C. Vahlas, A.G. Boudouvis, Multiscale modeling and experimental analysis of chemical vapor deposited aluminum films: linking reactor operating conditions with roughness evolution, Chem. Eng. Sci. 155 (2016) 449–458, https://doi.org/10.1016/j.ces.2016.08.039.

[38] Z.S. Khalifa, H. Lin, S. Ismat Shah, Structural and electrochromic properties of TiO_2 thin films prepared by metallorganic chemical vapor deposition, Thin Solid Films 518 (2010) 5457–5462, https://doi.org/10.1016/j.tsf.2010.04.013.

[39] R. Gonzalez, R. Zallen, H. Berger, Infrared reflectivity and lattice fundamentals in anatases, Phys. Rev. B Condens. Matter Mater. Phys. 55 (1997) 7014–7017, https://doi.org/10.1103/PhysRevB.55.7014.

[40] B.C. Trasferetti, C.U. Davanzo, R.A. Zoppi, N.C. da Cruz, M.A.B. de Moraes, Berreman effect applied to phase characterization of thin films supported on metallic substrates: the case of TiO_2, Phys. Rev. B 64 (2001) 125404–125411, https://doi.org/10.1103/PhysRevB.64.125404.

[41] C. Pecharromán, F. Gracía, J.P. Holgado, M. Ocaña, A.R. González-Elipe, J. Bassas, J. Santiso, A. Figueras, Determination of texture by infrared spectroscopy in titanium oxide-anatase thin films, J. Appl. Phys. 93 (2003) 4634–4645, https://doi.org/10.1063/1.1560858.

[42] N. Primeau, C. Vautey, M. Langlet, The effect of thermal annealing on aerosol-gel deposited SiO_2 films: a FTIR deconvolution study, Thin Solid Films 310 (1997) 47–56, https://doi.org/10.1016/S0040-6090(97)00340-4.

[43] L. Ferretto, A. Glisenti, Surface acidity and basicity of a rutile powder, Chem. Mater. 15 (2003) 1181–1188, https://doi.org/10.1021/cm021269f.

[44] C. Morterra, An infrared spectroscopic study of anatase properties, J. Chem. Soc. Faraday Trans. 1 (84) (1988) 1617–1637, https://doi.org/10.1039/F19888401617.

[45] L. Borgese, E. Bontempi, M. Gelfi, L.E. Depero, P. Goudeau, G. Geandier, D. Thiaudire, Microstructure and elastic properties of atomic layer deposited TiO_2 anatase thin films, Acta Mater. 59 (2011) 2891–2900, https://doi.org/10.1016/j.actamat.2011.01.032.

[46] N. Rahmani, R.S. Dariani, Strain-related phenomena in TiO_2 nanostructures spin-coated on porous silicon substrate, Superlattice. Microst. 85 (2015) 504–509, https://doi.org/10.1016/j.spmi.2015.05.048.

[47] A.S. Ferlauto, G.M. Ferreira, J.M. Pearce, C.R. Wronski, R.W. Collins, X. Deng, G. Ganguly, Analytical model for the optical functions of amorphous semiconductors from the near-infrared to ultraviolet: applications in thin film photovoltaics, J. Appl. Phys. 92 (2002) 2424–2436, https://doi.org/10.1063/1.1497462.

[48] D. Barreca, A. Gasparotto, C. Maccato, C. Maragno, E. Tondello, TiO_2 thin films by chemical vapor deposition: an XPS characterization, Surf. Sci. Spectra 14 (2010) 27–33, https://doi.org/10.1116/11.20070902.

[49] M. Horprathum, P. Eiamchai, P. Limnonthakul, N. Nuntawong, P. Chindaudom, A. Pokaipisit, P. Limsuwan, Structural, optical and hydrophilic properties of nanocrystalline TiO_2 ultra-thin films prepared by pulsed dc reactive magnetron sputtering, J. Alloys Compd. 509 (2011) 4520–4524, https://doi.org/10.1016/j.jallcom.2011.01.038.

[50] S. Ratzsch, E.-B. Kley, A. Tünnermann, A. Szeghalmi, Influence of the oxygen plasma parameters on the atomic layer deposition of titanium dioxide, Nanotechnology 26 (2015) 24003–24013, https://doi.org/10.1088/0957-4484/26/2/024003.

[51] X. Chen, S. Shen, L. Guo, S.S. Mao, Semiconductor-based photocatalytic hydrogen generation, Chem. Rev. 110 (2010) 6503–6570, https://doi.org/10.1021/cr1001645.

[52] N. Murakami, Y. Kurihara, T. Tsubota, T. Ohno, Shape-controlled anatase titanium (IV) oxide particles prepared by hydrothermal treatment of peroxo titanic acid in the presence of polyvinyl alcohol, J. Phys. Chem. C 113 (2009) 3062–3069, https://doi.org/10.1021/jp809104t.

[53] J. Yu, J. Low, W. Xiao, P. Zhou, M. Jaroniec, Enhanced photocatalytic CO_2-reduction activity of anatase TiO_2 by Coexposed {001} and {101} facets, J. Am. Chem. Soc. 136 (2014) 8839–8842, https://doi.org/10.1021/ja5044787.

[54] N. Roy, Y. Sohn, D. Pradhan, Synergy of low-energy {101} and high-energy {001} TiO_2 crystal facets for enhanced photocatalysis, ACS Nano 7 (2013) 2532–2540, https://doi.org/10.1021/nn305877v.

[55] J. Chen, H. Bin Yang, H.B. Tao, L. Zhang, J. Miao, H.Y. Wang, J. Chen, H. Zhang, B. Liu, Surface rutilization of anatase TiO_2 nanorods for creation of synergistically bridging and fencing electron highways, Adv. Funct. Mater. 26 (2016) 456–465, https://doi.org/10.1002/adfm.201504105.

[56] J. Chen, H.B. Tao, B. Liu, Unraveling the intrinsic structures that influence the transport of charges in TiO_2 electrodes, Adv. Energy Mater. 7 (2017) 1700886–1700915, https://doi.org/10.1002/aenm.201700886.

[57] Z. Fang, Y. Hong, D. Li, B. Luo, B. Mao, W. Shi, One-Step Nickel Foam Assisted Synthesis of Holey G-Carbon Nitride Nanosheets for Efficient Visible-Light Photocatalytic H_2 Evolution, ACS Appl. Mater. Interfaces 10 (2018) 20521–20529, https://doi.org/10.1021/acsami.8b04783.